1376 *Chem. Mater.* **2010,** *22,* 1376–1385
DOI:10.1021/cm9021535

CHEMISTRY OF MATERIALS
Article

Methylmagnesium Alkoxide Clusters with Mg_4O_4 Cubane- and Mg_7O_8 Biscubane-Like Cores: Organometallic Precursors for Low-Temperature Formation of MgO Nanoparticles with Variable Surface Defects

Stephan Heitz,[†] Yilmaz Aksu,[†] Christoph Merschjann,[‡] and Matthias Driess*,[†]

[†]*Institute of Chemistry: Metalorganics and Inorganic Materials, Technische Universität Berlin, Strasse des 17 Juni 135, D-10623 Berlin, Germany, and* [‡]*Institute for Heterogeneous Material Systems, Helmoltz-Zentrum Berlin für Materialien und Energie GmbH, Hahn-Meitner Platz 1, D-14109 Berlin, Germany*

Received July 16, 2009. Revised Manuscript Received November 26, 2009

Nanocrystalline MgO powders with variable surface defect concentrations are simply accessible by solid-state thermolysis at relatively low temperatures utilizing the molecular single-source precursors (SSPs) $[MeMgOR]_4$ ($R = {}^{i}Pr, {}^{t}Bu, {}^{Cy}Hex$) and the first bis-cubanes $Me_6Mg_7(OR)_8$ (Et, Pr, Bu). The decomposition conditions including heating rates, tempering times, and atmospheres have been varied, and the structure and purity of the obtained samples were analyzed by means of different analytical techniques (TGA, PXRD, TEM, EDX, elemental analysis and BET measurements). The crystal sizes vary from approximately 8 to 15 nm depending on the heating rates, tempering times and nature of the applied SSP. Photoluminescence spectroscopy (PLS) of the samples suggests the presence of defects, which could be attributed to different surface oxide sites of the MgO particles depending on the thermolysis conditions, in particular the heating rate and tempering time.

Introduction

Metal-oxide-based nanomaterials have attracted considerable interest due to their wide range of applications, including their key role in heterogeneous catalysis and as ingredients for the preparation of advanced structural ceramics.[1] Because of its distinguished properties such as a low dielectric constant, a low refractive index, an excellent thermal and chemical stability as well as a high thermal conductivity, MgO is one of the most intensively investigated oxidic materials.[2] It is widely used as inorganic material in diverse areas such as fire resistant construction materials,[3] optical materials,[4] protective layers in plasma display panels,[5] and buffer layers for thin films.[6] In addition, MgO shows catalytic activity in numerous promising chemical transformations, e.g., oxidative coupling of methane (OCM),[7] the Tishchenko reaction,[8] and transfer hydrogenations.[9] However, the knowledge on the catalytic function of MgO on the molecular scale is still scarce. As expected, the material properties of MgO are strongly influenced by its morphology and defect structure, which can be changed significantly through sizing from bulk to nano dimensions.[10] To study structure−activity−selectivity relationships of MgO substrates, it is highly desirable to facilitate a straightforward access to pure MgO nanoparticles with tunable defects even at low temperature. However, the classical approach to MgO utilizing inorganic precursors such as carbonates, nitrates and hydroxides, requires drastically high decomposition temperatures up to 1000 °C, and allows only a feeble control on the material properties.[11]

Organometallic single-source precursors (SSPs) offer a promising alternative to the classical preparation methods.[12a−d] SSPs consist of small molecular building blocks, which contain the respective elements of the desired material in the required ratio. One of the additional advantages using SSPs is that they can be volatile and decomposed at relatively low temperature. Additionally,

*Corresponding author. E-mail: matthias.driess@tu-berlin.de.

(1) Venkateswara Rao, K.; Sunandana, C. S. *J. Mater. Sci.* **2008**, *43*, 146.
(2) Durusory, H. Z. *J. Mater. Sci. Lett.* **1991**, *10*, 1023.
(3) (a) Jansen, H. PCT WO2008107343 (A1). (b) Frobosilo, R. C.; Borgia, S.; Lindner, M. U.S. Pat. Appl. Publ. 20080178782.
(4) Hiroo, K.; Osaka, O.; Mikio, S.Patents Abstracts of Japan 2005−258028.
(5) (a) Okada, T.; Komaki, T. *Jpn. J. Appl. Phys.* **2008**, *47*, 1699–1705. (b) Kim, K. D.; Park, Y. S. U.S. Pat. Appl. Publ. 20070069989 (A1). (c) Lee, K. W.; Chung, J. S. U.S. Pat. Appl. Publ. 20070035248 (A1).
(6) Sung, M. M.; Kim, C. G.; Kim, J.; Kim, Y. *Chem. Mater.* **2002**, *14*, 826–831.
(7) Driscoll, D. J.; Martir, W.; Wang, J. X.; Lunsford, J. H. *J. Am. Chem. Soc,.* **1985**, *107*, 58.
(8) Tsuji, H.; Hattori, H. *Catal. Today* **2006**, *116*, 239.
(9) Szöllösi, G.; Bartók, M. *Appl. Cat. A: General* **1998**, 263.
(10) Lucas, E.; Decker, S.; Khaleel, A.; Seitz, A.; Fultz, S.; Ponce, A.; Li, W.; Carnes, C.; Klabunde, K. J. *Chem.—Eur. J.* **2001**, *7*, 2505.
(11) (a) Green, J. *J. Mater. Sci.* **1983**, *18*, 637. (b) Alvarado, E.; Torres-Martinez, L. M. *Pholyhedron* **2000**, *19*, 2345.
(12) (a) Caulton., K. G.; Hubert-Pfalzgraf, L. G. *Chem. Rev.* **1990**, *90*, 969–995. (b) Veith, M.; Mathur, S.; Mathur, C. Polyhedron **1998**, *17*(5−6), 1005−1034 and cited ref. therein. (c) Orlov, A.; Roy, A.; Lehmann, M.; Driess, M.; Polarz, S. *J. Am. Chem. Soc.* **2007**, *129*, 371–375. (d) Aksu, Y.; Driess, M. *Angew. Chem., Int. Ed.* **2009**, *121*, 7918. (e) Mathur, S.; Driess, M. *Comprehensive Organometallic Chemistry III*; Crabtree, R. H., Mingos D. M. P., Eds.; Elsevier: Oxford, U.K., 2007; pp 35−70.

Published on Web 02/01/2010

even subtle changes in the mild thermolysis conditions and of the (organic) leaving groups (terminal substituents) of the precursor can lead to significantly different materials due to the presence of defects.[12e]

Although several SSPs for metalorganic chemical vapor deposition (MOCVD) of MgO thin films have been described in the literature,[13] there is merely one report on the preparation of MgO powders using magnesium alcoholates as SSPs.[14] The MgO samples obtained from the aformentioned molecular SSPs were merely analyzed with respect to their purity and morphology, but no studies on the presence of defects or the influence of different decomposition parameters on the properties of the final product have been reported.

Currently, it is well-documented that alkylzinc alkoxide clusters $(RZnOR')_4$ with a Zn_4O_4 core are excellent SSPs for the preparation of ZnO nanoparticles with different defects[15] that represent another class of seemingly simple metal oxide substrates utilized in heterogeneous catalysis. The latter results prompted us to investigate whether MgO nanoparticles are accessible employing analogous alkylmagnesium alkoxide clusters $(RMgOR')_4$ as SSPs. Here we wish to report the facile synthesis of MgO nanoparticles with variable surface defects employing methylmagnesium alkoxide clusters with Mg_4O_4 cubane cores. Additionally, we report on a novel type of suitable SSPs for MgO, nameley the first mixed magnesium-methylmagnesium alkoxo clusters having an Mg_7O_8 core.

Results and Discussion

SSP Syntheses. Alkylmagnesium alkoxides are easily accessible by Brønsted-acid−base reactions between alcohols and dialkylmagnesium compounds and tend to oligomerize via intermolecular O—Mg donor−acceptor bonds. In 1968, Coates and co-workers investigated by means of cryoscopy and elemental analysis that their grade of association depends on the polarity of the solvent.[14] In coordinating solvents, such as tetrahydrofuran and ether, alkylmagnesium alkoxides form dimeric solvates, whereas applying benzene as solvent leads to unsolvated tetramers and oligomers. A further investigation of the association grade by Ashby and co-workers showed that complex equilibria between different oligomeric and dimeric forms take place in coordinating solvents.[16]

Scheme 1. Synthesis of 1a−c and 2a−c

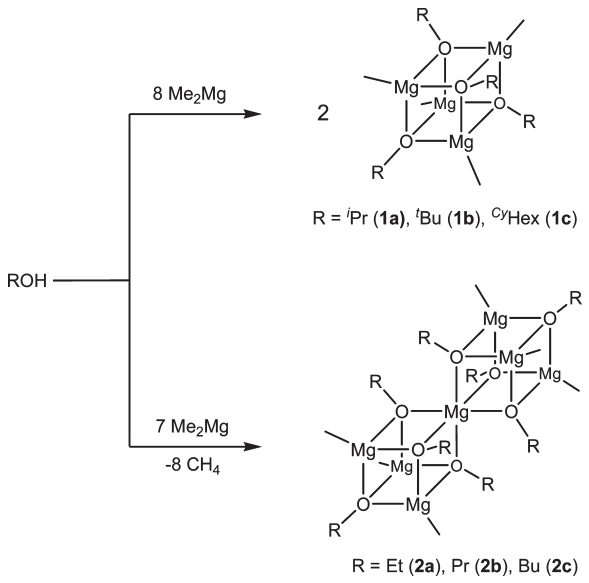

To suppress dissociation equilibria, we carried out the synthesis of methylmagnesium alkoxide clusters in toluene as least coordinating solvent. As the association grade of methylmagnesium alkoxides mainly depends on the steric demand of the alkoxy group,[16,17] we investigated the conversion of dimethylmagnesium, Me_2Mg, with different branched and linear alcohols.

Me_2Mg reacts with sterically congested alcohols ROH (R = ^{i}Pr, ^{t}Bu, ^{Cy}Hex) in the molar ratio of 1:1 to give the heterocubanes $[MeMgOR]_4$ (**1a−c**) (Scheme 1). The latter can be isolated in 42 (**1a**), 58 (**1c**), and 98% yield (**1b**), along with insoluble higher aggregated side-products. Similar compounds such as $[(C_5H_5)MgOEt]_4$,[18] $[MeMgO^tBu]_4$,[19] and $[(Me_3SiCH_2)Mg(OCH_2SiMe_3)]_4$[20] are already known and have been spectroscopically and structurally characterized by other research groups.

Linear alcohols ROH (R = Et, Pr, Bu) undergo conversion with Me_2Mg in the molar ratio of 8:7 to form the $Me_6Mg_7(OR)_8$ biscubanes **2a**, **2b**, and **2c** which can be isolated in 78, 96, and 74% yield, respectively, instead of the expected Mg_4O_4 cubanes. To the best of our knowledge, **2a−c** are the first examples for Mg_7O_8 biscubanes structurally characterized. Previous cryoscopic measurements

(13) (a) Zeng, J. M.; Wang, H.; Shang, S. X.; Wang, Z.; Wang, M. *J. Cryst. Growth* **1996**, *169*, 474. (b) Boo, J. H.; Lee, S. B.; Yu, K. S.; Koh, W.; Kim, Y. *Thin Solid Film* **1999**, *341*, 63. (c) Davies, H. O.; Jones, A. C.; Leedham, T. J.; Crosbie, M. J.; Wright, P. J.; Boag, N. M.; Thompson, J. R. *Chem. Vap. Deposition* **2000**, *6*(2), 71. (d) Sung, M. M.; Kim, C. G.; Kim, J.; Kim, Y. *Chem. Mater.* **2000**, *14*, 826. (e) Hill, M. R.; Jones, A. W.; Russell, J. J.; Roberts, N. K.; Lamb, R. N. *J. Mater. Chem.* **2004**, *14*, 3198. (f) Okada, T.; Komaki, T. *Jpn. J. Appl. Phys.* **2008**, *47*(3), 1699.

(14) Thoms, H.; Epple, M.; Viebrock, H.; Reller, A. *J. Mater. Chem.* **1995**, *5*(4), 589.

(15) (a) Hambrock, J.; Rabe, S.; Merz, K.; Birkner, A.; Wohlfahrt, A.; Fischer, R. A.; Driess, M. *J. Mater. Chem.* **2003**, *13*(7), 1731. (b) Boyle, T. J.; Bunge, S. D.; Andrews, N. L.; Matzen, L. E.; Sieg, K.; Rodriguez, M. A.; Headley, T. J. *Chem. Mater.* **2004**, *16*, 3279. (c) Ischenko, V.; Polarz, S.; Grote, D.; Stavarache, V.; Fink, K.; Driess, M. *Adv. Funct. Mater.* **2005**, *15*, 1945. (d) Schröder, D.; Schwarz, H.; Polarz, S.; Driess, M. *Phys. Chem. Chem. Phys.* **2005**, *7*, 1049. (e) Polarz, S.; Roy, A.; Merz, M.; Halm, S.; Schröder, D.; Schneider, L.; Bacher, G.; Kruis, F. E.; Driess, M. *Small* **2005**, *1*(5), 540. (f) Jana, S.; Aksu, Y.; Driess, M. *Dalton Trans.* **2009**, 1516. (g) Polarz, S.; Strunk, J.; Ischenko, V.; W. E. van den Berg, M.; Hinrichsen, O.; Muhler, M.; Driess, M. *Angew. Chem., Int. Ed.* **2006**, *45*(18), 2965. (h) Polarz, S.; Roy, A.; Lehmann, M.; Driess, M.; Kruis, F. E.; Hoffmann, A.; Zimmer, P. *Funct. Mater.* **2007**, *17*, 1385–1391.

(16) Ashby, E. C.; Nackashi, J.; Parris, G. E. *J. Am. Chem. Soc.* **1975**, *97* (11), 3162.

(17) Coates, G. E.; Heslop, J. A.; Redwood, M. E.; Ridley, D. *J. Chem. Soc., A* **1968**, *5*, 1118.

(18) Lehmkuhl, H.; Mehler, K.; Benn, R.; Rufinska, A.; Krüger, C. *Chem. Ber.* **1986**, *119*(3), 1054.

(19) Sung, M. M.; Kim, C. G.; Kim, J.; Kim, Y. *Chem. Mater.* **2002**, *14*, 826.

(20) Moreno, C. A.; Hughes, D. L.; Bochmann, M. *Polyhedron* **2007**, *26*, 2523.

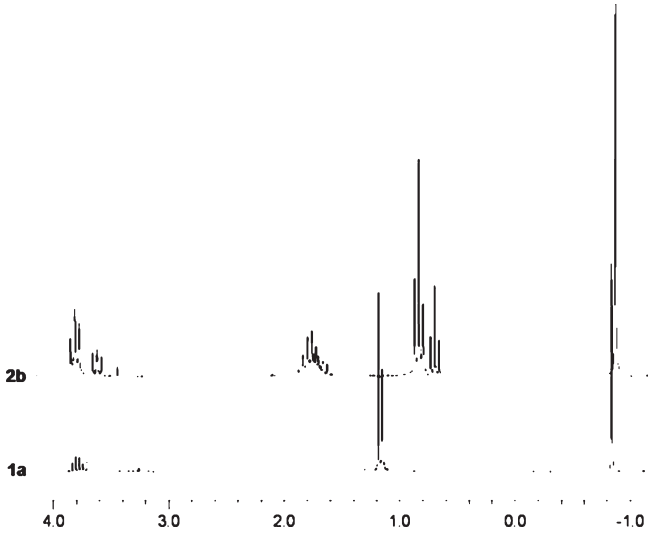

Figure 1. ^{1}H NMR-spectra of **1a** and **2b** in C_6D_6.

by Ashby et al. revealed that the degree of association (n) of $(MeMgOPr)_n$ is between 7 and 9 and thus a heptameric structure has been proposed.[16] Our results prove that the $Me_6Mg_7(OPr)_8$ biscubane **2b** crystallizes from solutions, instead of $[MeMgOPr]_n$ clusters.

All synthesized magnesium alkoxides are very sensitive toward air and moisture. Their constitutions are consistent with the respective ^{1}H and ^{13}C NMR data. The ^{1}H NMR spectra of the Mg_4O_4 cubane **1a** and the Mg_7O_8 biscubane **2b** are displayed in Figure 1. Because the alkoxide groups in monocubanes are chemically equivalent, the ^{1}H NMR spectrum of **1a** exhibits only one set of signals for the *i*-propoxide groups. However, the biscubanes **2b** contains two chemically different sorts of isopropoxy groups. The six alkoxide groups which are directly connected to the central Mg atom, appear at lower field than the remaining alkoxides on the opposite of the central Mg atom.

Single crystals of all alkoxides (**1a**−**c**; **2a**−**c**) were obtained by crystallization in *n*-hexane at −20 °C. As a result of poor single-crystal qualities of **1b**,**c** and **2a**,**c**, respectively, only the crystal structures of **1a** and **2b** are discussed here. Compound **1a** crystallizes in the monoclinic space group $P2/n$, whereas compound **2b** is triclinic (space group $P\bar{1}$). Their molecular structures determined by X-ray diffraction analysis are shown in Figures 2 and 3, respectively. Selected bond distances and angles are summarized in Table 1. The structure of **1a** is similar to that other heterocubanes[19,20] and consists of a distorted Mg_4O_4 cluster core. The Mg−O—Mg angles are smaller than 90° (85−86°), whereas the O−Mg—O angles are a little larger than 90° (92−93°). The molecular structure of **2b** resembles that of the analogous biscubanes with a Zn_7O_8 core.[21]

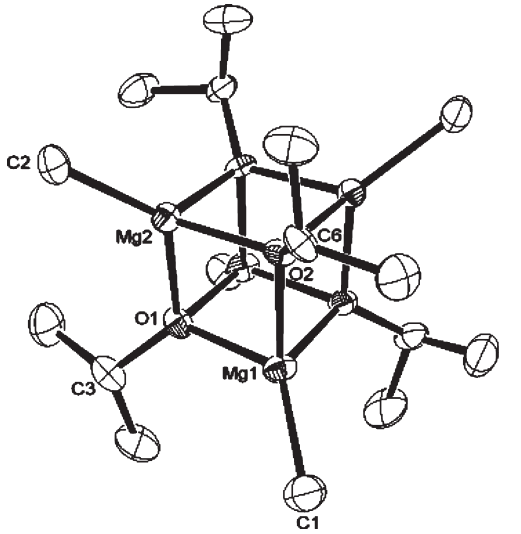

Figure 2. Molecular Structure of $[MeMgO^iPr]_4$ **1a**. Thermal ellipsoids are drawn at the 50% probability level. The hydrogen atoms are omitted for clarity. For selected distances and angles, see Table 1.

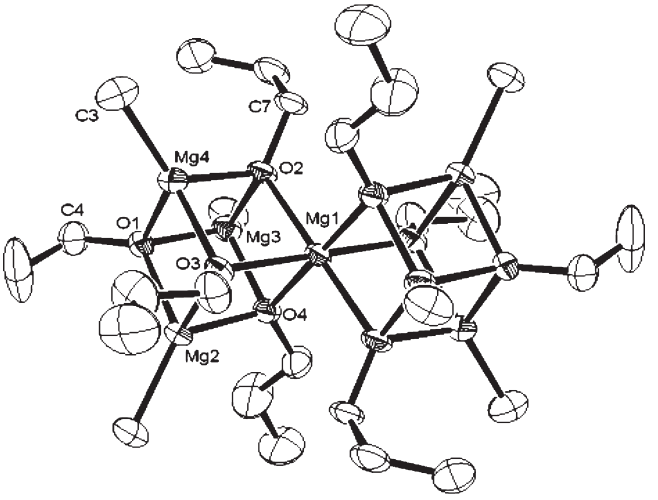

Figure 3. Molecular structure of $Me_6Mg_7(OPr)_8$ **2b**. Thermal ellipsoids are drawn at the 50% probability level. The hydrogen atoms are omitted for clarity. For selected distances and angles, see Table 1.

The topology of **2b** can be simplified described as two Mg_4O_4 cubes which are connected to each other via a shared Mg ion. The latter is octahedrally surrounded by six oxygen atoms and represents a center of symmetry. Each heterocubane partial core of the biscubane is more distorted than the Mg_4O_4 cubes in monocubanes (i.e., of

(21) (a) Ziegler, M. L.; Weiss, J. *Angew. Chem., Int. Ed.* **1970**, *9*, 905. (b) Ishimori, M.; Hagiwara, T.; Tsuruta, T.; Kai, Y.; Yasuoka, N.; Kasai, N. *Bull. Chem. Soc. Jpn.* **1976**, *49*(4), 1165. (c) Boyle, T. J.; Bunge, S. D.; Andrews, N. L.; Matzen, L. E.; Sieg, K.; Rodriguez, M. A.; Headley, T. J. *Chem. Mater.* **2004**, *16*, 3279. (d) Polarz, S.; Neues, F.; van den Berg, M. W. E.; Grünert, W.; Khodeir, L. *J. Am. Chem. Soc.* **2005**, *127* (34), 12028. (e) Jana, S.; Berger, R.; Fröhlich, R.; Pape, T.; Mitzel, N. W. *Inorg. Chem.* **2007**, *46*, 4293.

(22) Coluccia, S.; Marchese, L.; Lavagnino, S.; Anpo, M. *Spectrochim. Acta, A* **1987**, *43*(12), 1573.
(23) (a) Coluccia, S.; Deane, A. M.; Tench, A. J. *J. Chem. Soc. Faraday Trans. I* **1978**, *74*, 2913. (b) Coluccia, S.; Tench, A. J.; Segall, R. *J. Chem. Soc., Faraday Trans. I* **1979**, *75*, 1769.
(24) Anpo, M.; Yamada, Y.; Kubokawa, Y.; Coluccia, S.; Zecchina, A.; Che, M. *J. Chem. Soc., Faraday Trans. I* **1988**, *84*, 751.
(25) Bailly, M. L.; Costentin, G.; Pernot, H. L.; Krafft, J. M.; Che, M. *J. Phys. Chem. B* **2005**, *109*, 2404.
(26) Chizallet, C.; Costentin, G.; Pernot, H. L.; Krafft, J. M.; Che, M.; Delbecq, F.; Sautet, P. *J. Phys. Chem. C* **2008**, *112*, 16629.
(27) Benia, H. M. Ph.D. Thesis. Humboldt Universität Berlin, Germany, 2008.
(28) García, J. A.; Remón, A.; Piqueras, J. *Solid State Commun.* **1986**, *58*(8), 555.
(29) Lühder, K.; Nehls, D.; Madeja, K. *J. Prakt. Chem.* **1983**, *325*(6), 10.

Table 1. Selected Distances (Å) and Angles (deg) of 1a and 2b

1a		2b	
Mg(1)−O(1)	2.056(4)	Mg(1)−O(3)	2.1016(17)
Mg(1)−O(2)	2.057(4)	Mg(1)−O(2)	2.1144(17)
Mg(2)−O(1)	2.044(4)	Mg(1)−O(4)	2.1155(18)
Mg(2)−O(2)	2.042(3)	Mg(2)−O(1)	2.048(2)
O(1)−Mg(1)−O(2)	85.88(16)	Mg(2)−O(3)	2.039(2)
O(2)−Mg(2)−O(1)	86.59(17)	Mg(2)−O(4)	2.035(2)
Mg(2)−O(1)−Mg(1)	93.27(17)	O(3)−Mg(1)−O(2)	81.98(7)
Mg(2)−O(2)−Mg(1)	93.28(17)	O(4)−Mg(2)−O(1)	85.44(8)
		Mg(2)−O(1)−Mg(3)	93.95(8)
		Mg(3)−O(2)−Mg(1)	96.12(8)

1a). Likewise, the Mg−O—Mg angles in **2b** are smaller than 90° (81−85°) and the O−Mg—O angles exceed 90° (94−96°).

Solid-State Decomposition of the Precursors. Thermolyses of the methylmagnesium alkoxide clusters **1a**−**c** and **2a**−**c** lead to nanocrystalline MgO and its respective formation was initially examined by TGA/DTG studies (see the Supporting Information, SI-3a-e). All precursors (**1a**−**c**, **2a**−**c**) were decomposed under standard conditions (5 K min^{-1}, from 25 to 600 °C) under dry synthetic air (20% O_2, 80% N_2), affording colorless MgO samples. Additionally, we investigated in particular the formation of MgO derived from the degradation of **1b** in different atmospheres (O_2 concentrations), applying different heating rates and holding time at 600 °C. The respective TGA and DTG curves for **1b** under dry synthetic air (20% O_2, 80% N_2) are shown in Figure 4a.

The TGA curve for **1b** displays a marginal weight gain of 0.7% at the very beginning of the degradation, which is likely to be caused by preoxidation of the precursor. The main mass loss starts at 190 °C and is finished at around 480 °C. This results in a final loss of 33.39%, which agrees well with the calculated value for complete conversion to MgO (35.84%) (Table 2). The TGA and DTG curves for the degradation of the monocubanes **1a** and **1c** under same experimental conditions are similar to those observed for **1b** (see the Supporting Information SI-3a-b). The decomposition of the precursors involves several degradation processes including reductive elimination of the organic groups at magnesium and oxygen to give methane and respective olefins as well as oxidation of the organic components to carbon oxides and water. Accordingly, the degradation of **1b** monitored by TGA-MS (see the Supporting Information SI-4b) shows that CH_4 evolves at relatively low temperatures (~150 °C). In addition isobutene (*m*/*e* 56) was detected in the gas phase at ~260 °C, produced probably from the decomposition of residual *tert*-butoxide groups. Isobutene undergoes typically further conversion into CH_4 (*m*/*e* 16) and C_3H_4 (*m*/*e* 40). At around 400 °C, H_2O and CO_2 were mainly observed indicating the complete oxidation of the residual organics (see the Supporting Information SI-4b). The TGA-MS of **1a** displays similar characteristics with the difference being that in the TGA-MS of **1a**, acetone (*m*/*e* 58) and its acetyl fragment (*m*/*e* 43) were detected (see the Supporting Information SI-4a) instead of isobutene, which is typical for the decomposition of metal isopropoxides.[15d]

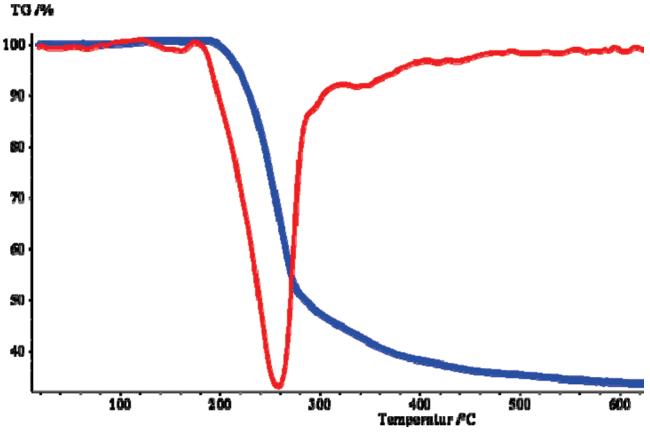

Figure 4a. TGA and DTG curves for the decomposition of [MeMgO^{t}Bu]$_4$ **1b** in dry synthetic air.

Table 2. Calculated and Experimentally Observed Mass Loss of 1a−c and 2a−c after Total Degradation to MgO

precursor	calculated remaining mass after total degradation to MgO (wt %)	experimental remaining mass after total degradation to MgO (wt %)
[MeMgO^{i}Pr]$_4$**1a**	40.95	38.36
[MeMgO^{t}Bu]$_4$**1b**	35.84	33.39
[MeMgO^{Cy}Hex]$_4$**1c**	29.10	27.96
$Me_6Mg_7OEt_8$**2a**	47.70	37.94
$Me_6Mg_7OPr_8$**2b**	40.04	36.50
$Me_6Mg_7OBu_8$**2c**	35.02	31.11

Two local minima of the DTG curve were observed at 257 and 318 °C in **2b**, showing that the degradation process occurs in several steps. **2a** and **2c** show comparable degradation characteristics; however, they differ slightly in the temperature range of the mass loss and the shape of the DTG curves. The TGA studies of the biscubanes **2a**−**c** resulted in remaining masses that were lower than the calculated ones for total degradation to MgO. This difference between the theoretical and experimental values is presumably due to partial formation of volatile magnesium containing intermediates formed during the decomposition of the precursors. The DTG curves of the biscubanes (**2a**−**c**) display higher maximum decomposition temperatures than those for the monocubanes (**1a**−**c**), consistent with a higher degree of association.[30] The higher temperature for complete degradation of the biscubanes (**2a**−**c**) also leads to an increase in evaporation of volatile magnesium containing intermediates produced through the degradation process, which could reason the lower yield of MgO.

The degradation and the resulting gas products from **2a**−**c** were further investigated by TGA-MS (for **2b**, see the Supporting Information, SI-4c). All three complexes exhibit similar TGA-MS spectra indicating mainly the formation of methane, water, and carbon dioxide with additional traces of hydrocarbon fragments (C_3 and C_4), which agree well with reported results for similar compounds.[15d]

(30) Davies, O- K.; Jones, A. C.; Leedham, T. J.; Crosbie, M. J.; Wright, P. J.; Boag, N. M.; Thompson, J. R. *Chem. Vap. Deposition* **2000**, *2*, 6.

Table 3. Investigated Decomposition Conditions for Precursors 1a−c and 2a−c

precursor	heating rate (K/min)	holding time at 600 °C (h)	oxygen concentration (vol %)	crystal size from Debye−Scherrer equation (nm)	BET-surface (m^2/g)	carbon impurities (wt %)
$[MeMgO^iPr]_4$**1a**	5	2	20	11.01	79.8	0.34
$[MeMgO^tBu]_4$**1b**	5	2	20	10.23	108.2	0.26
$[MeMgO^{Cy}Hex]_4$**1c**	5	2	20	13.78	81.6	1.61
$Me_6Mg_7OEt_8$**2a**	5	2	20	13.56	72.3	0.22
$Me_6Mg_7OPr_8$**2b**	5	2	20	10.73	93.0	0.37
$Me_6Mg_7OBu_8$**2c**	5	2	20	11.62	77.5	0.20
$[MeMgO^tBu]_4$**1b**	1	2	20	9.62	117.3	0.12
1b	3	2	20	9.89	116.4	0.17
1b	10	2	20	10.45	80.1	0.41
1b	20	2	20	12.01	88.5	0.42
1b	5	0	20	8.73	126.2	0.18
1b	5	2	20	10.23	108.2	0.26
1b	5	4	20	13.08	52.9	0.16
1b	5	8	20	15.54	21.1	0.24
1b	5	2	20	10.23	108.2	0.26
1b	5	2	50	10.29	109.7	0.20
1b	5	2	75	10.01	114.9	0.19
1b	5	2	0	18.45	73.9	7.00

The degradation of the magnesium alkoxide clusters (**1a-c**, **2a-c**) under exclusion of dioxygen in a dinitrogen atmosphere (for **1b**, see the Supporting Information SI-4d and SI-5a) also leads to nanocystalline MgO. Although the latter materials are black because of the relatively large carbon impurities,[15d] their PXRD profiles show only the MgO pattern (see the Supporting Information SI-5b). In the case of **1b**, the resulting "black" MgO possesses a carbon impurity of 7 wt % (Table 3). The degradation of **1b** was also studied applying different heating rates, dioxygen concentrations, and tempering times. The respective decomposition conditions, crystal sizes, and the specific BET (Brunauer−Emmet−eller) surface areas measured using nitrogen adsorption at 77 K are summarized in Table 3.

The PXRD patterns (Figure 5; see also the Supporting Information SI-6a-b) of the samples exhibit MgO as the only crystalline phase present in the remaining materials. The broad reflexes indicate that very small MgO particles were formed. The corresponding crystal sizes were calculated from the full width at half-maximum (fwhm) of PXRD patterns by applying the Debye−Scherrer equation to the isolated reflex centered at $2\theta = 42.9°$ corrected for instrumental broadening. The crystal size differs from 10.2 to 13.8 nm, depending on the used precursor (Table 3). Štengl et al. investigated the ultrasound enhanced hydrolysis of magnesium methoxide and magnesium ethoxide leading to MgO agglomerates of isometric nanoparticles with crystal size of 10 nm, which compares well with our results. However, the reported large specific surface area of 1236 m^2/g reveals the fundamental effect of ultrasound on the specific surface of the MgO precipitates.[31] A similar study on the crystallization behavior of nanosized MgO particles from magnesium alkoxides reported by Jung et al. demonstrated that the difference in the size of the alkoxy group seems to play an important role for the crystal size of the final product. For example, the crystallite sizes of MgO prepared from magnesium methoxide and magnesium ethoxide were 14.8 and 26.5 nm, respectively.[32]

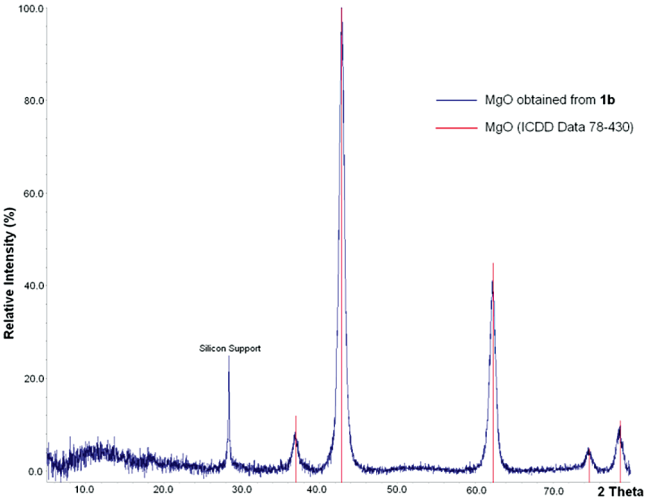

Figure 5. PXRD pattern of MgO derived from the degradation of $[MeMgO^tBu]_4$ (**1b**) in synthetic air (RT → 600 °C (2 h); heating rate 5 K/min).

Interestingly, a similar trend can be observed for our series of precursors. Thus, the MgO crystal size produced from the precursors **1a**−**c** degreases with increasing steric demand of the alkoxy groups in the precursor in the order of **1a** > **1c** > **1b** (Table 3). Likewise, the MgO particles formed from **2b** (ca. 10.7 nm) are smaller than those from **2c** (ca. 11.6 nm) and **2a** (ca. 13.6 nm), indicating that larger alkoxy groups lead to smaller MgO particles. In addition, the crystal size of the MgO samples coincide well with the specific surface areas, that is, samples consisting of small particles have larger specific surface areas (**1b**), whereas larger MgO particles lead to lower surface areas (**2a**) (Table 3). However, a quantitative correlation between the steric demand of the alkoxy groups in a precursor, crystal size, and specific surface area of the resulting MgO materials could not be deduced.

(31) Štengl, V.; Bakardijieva, S.; Maříková, M.; Bezdička, P.; Šubrt, J. *Mater. Lett.* **2003**, *57*, 3998.

(32) Jung, H. S.; Lee, J.-K.; Kim, J.-Y.; Hong, K. S. *J. Colloid Interface Sci.* **2003**, *259*, 127.

Besides the employment of different organometallic precursors for the formation of varying MgO nanoparticles by degradation of the precursors in the presence of O_2, the crystal size seems to be influenced by two other factors: the heating rate and the tempering time. For example, a slow heating rate affords smaller particles. The variation in the heating rate for the degradation of **1b** in the presence of O_2 from 1 to 20 K/min leads to particles with an average size between ca. 9.6 and 12.0 nm and corresponding BET surface areas between ca.117 and 88 m^2/g, respectively. As expected, prolonged annealing leads to agglomeration of the nanoparticles and thus furnishes on average, larger particles. When **1b** was decomposed and subsequently calcinated for longer times at 600 °C, the average crystal size is increased from ca. 8.7 to 15.5 nm after 8 h. Correspondingly, the BET surface areas agree well with this trend as they drop from ca. 126 to 21 m^2/g. In addition, low O_2 concentrations have also a marked influence on the crystal size as shown by the degradation of **1b** in pure nitrogen. The latter process leads to MgO samples (proven by PXRD; see the Supporting Information, 5b) which appears black because of the high impurity concentrations of amorphous carbon (Table 3). However, the formation of MgO even in absence of O_2 proves that **1b** serves faithfully as a SSP.

The CO_2 and H_2O produced during the thermal degradation of the precursors could partially adsorb at the yielded MgO nanoparticles to form carbonate and terminal OH sites at the surface. It turned out that the amount of carbon impurity in the MgO powders can depend on the nature of the organic substitutents at the alkoxy groups in the precursor.

The presence of carbon impurities and terminal OH groups in the obtained MgO powders were determined by means of elemental analysis (Table 3) and IR spectroscopy. Most of the samples listed in Table 3 contain less than 0.4 wt % carbon, except for the "black" MgO with 7 wt % carbon impurity that results from degradation of **1b** in pure nitrogen atmosphere. With merely 0.2 wt % carbon impurity, **1a**, **2a**, and **2c** proved to be the precursors of choice for a nonwet preparation of nanocrystalline MgO in dry synthetic air. In contrast, $[MeMgO^{Cy}Hex]_4$ **1c** is the least suitable precursor in this series with up to 1.6 wt % carbon impurity which also causes a gray appearance of the samples. The relatively high carbon content is due to incomplete digestion of the cyclohexyl group, leading to elemental carbon and carbonates. Remarkably pure (colorless) MgO samples with only 0.12 wt % carbon (determined by elemental analysis) can be obtained upon decomposition of **1b** with heating rates below 5 K/min. It has been shown that low heating rates facilitate complete removal and decomposition of the organic components around the precursor and thus prevent the formation of undesired organic byproduct.

According to the characteristic vibration bands between 1300 and 1500 cm^{-1} in the IR spectra, the carbon content can be assigned to carbonate. No other impurity could be detected by IR spectroscopy. Two kinds of OH vibration bands can be detected between the range of 3000 and 3800 cm^{-1}: (i) associated OH groups, which are involved in hydrogen bonds with neighbors, indicated by a broadband between 3000 and 3800 cm^{-1}, and (ii) a sharp vibration mode at 3700 cm^{-1}, which can be assigned to "isolated" terminal OH groups at the MgO surface.[22]

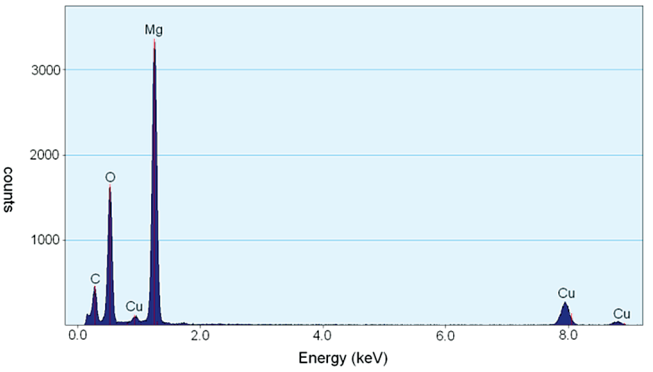

Figure 6. EDX profile of a MgO sample prepared from **1b** (20% O_2; 80% N_2; RT → 600 °C (2 h); 5 K/min).

EDX measurements (see the Supporting Information SI-7) performed on different MgO samples (e.g., from **1b**; see Figure 6) showed magnesium and oxygen as the only elements in the materials.

TEM examinations (Figure 7a−d, see also Supporting Information SI-8a, 8b, 8c) of the MgO samples prepared by thermal degradation of different magnesium alkoxide clusters in dry synthetic air showed no significant differences in size and crystallinity of the product particles. MgO nanoparticles prepared at high temperature (1170 K) under high vacuum (5×10^{-6} mbar) attain an almost perfect cubic shape.[34] Figure 7c,d (see also Supporting Information SI-8a-c) shows low-magnification TEM images of as-prepared MgO samples, displaying a fairly uniform distribution of the nanoparticles and their tendency to form agglomerates.

It is shown from high-resolution TEM (HRTEM) images (Figure 7b,e and the Supporting Information SI-8b-c) that the MgO agglomerates consist of irregularly shaped nanoparticles indicating a large amount of defect structures on the surface. These surface defects and the particle interactions resulting from van der Waals and electrostatic forces enable the MgO nanoparticles to form agglomerates. Furthermore, the intermolecular hydrogen bonding of the hydroxyl groups present on the particle surfaces (see above) can also interconnect the MgO nanoparticles to networks.

The average crystal size obtained from TEM micrographs for MgO samples prepared by standard conditions ranges from ca. 8 to 10 nm, which is consistent with the PXRD data. Imaging at high resolution shows lattice spacings of MgO, e.g. from {200}-planes with $d = 0.21$ nm (Figure 7e). There are no visible differences between particles prepared under different conditions.

(33) Sheldrick, G. M., *SHELXL-97, Program for Crystal Structure Refinement*; University of Göttingen: Göttingen, Germany, 1997.
(34) Stankic, S.; Mueller, M; Diwald, O.; Sterrer, M.; Knoezinger, E.; Bernardi, J. *Angew. Chem., Int. Ed.* **2005**, *44*, 4917.

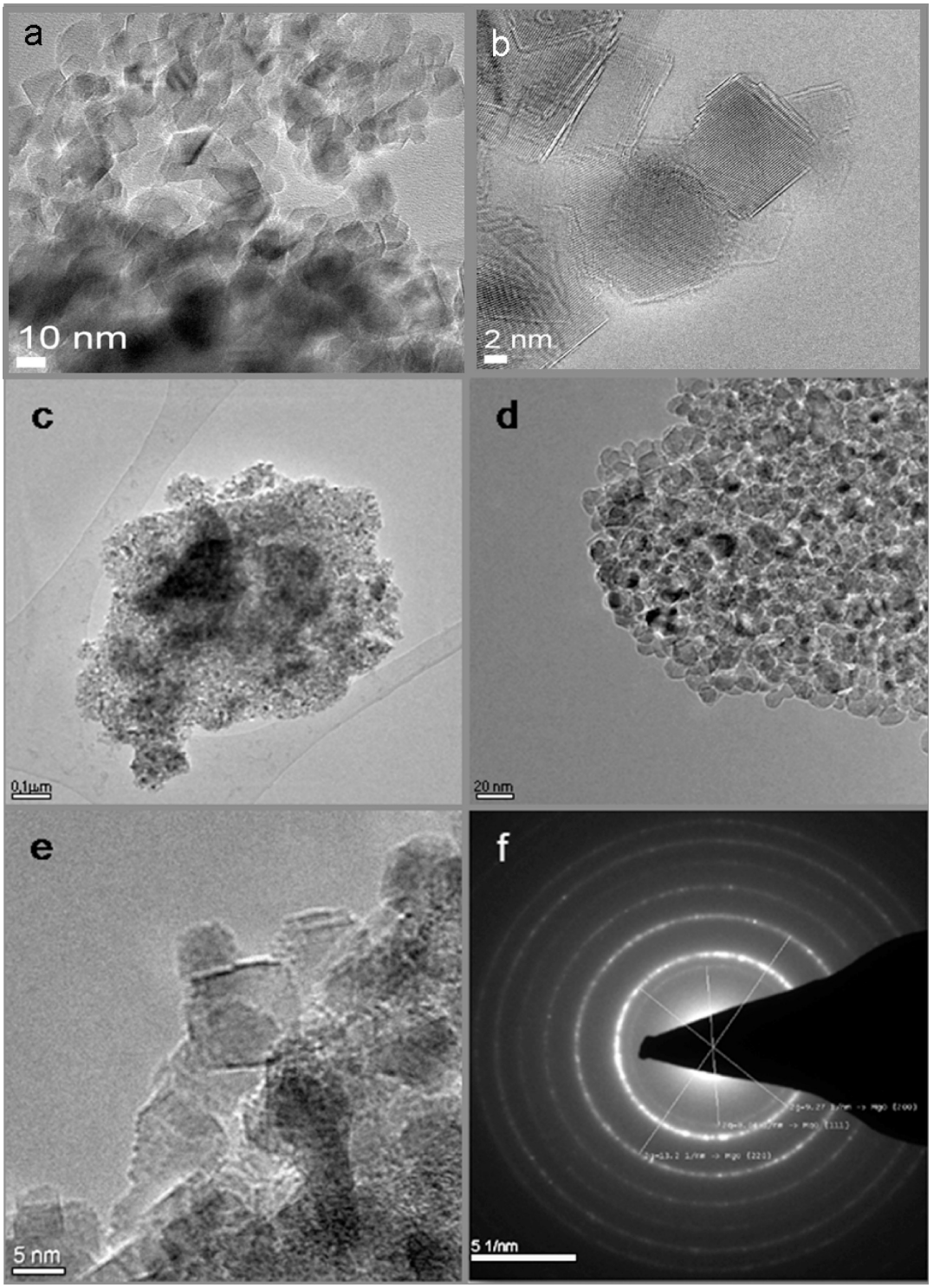

Figure 7. (a, b) TEM images of MgO nanopowders prepared from **1b**; (c, d) TEM images of MgO particles prepared from **2b**; (e) HRTEM image of MgO particles prepared from **2b**; (f) Selected-area electron diffraction pattern of MgO prepared from **1b**.

Separation of the nanoparticles by treatment with supersonic waves did not have a significant effect. The presence of clear diffraction rings at the PXRD pattern (Figure 7f) proves the crystallinity of the samples. The reciprocal lengths of the rings coincide well with MgO (NaCl structure, fcc, $a = 0.4212$) within the tolerance error (~5%).

Photoluminescence spectroscopy (PLS) was applied in order to show the presence of variable surface defects of the samples.[25,26] The PL spectroscopy is one of the few methods to detect oxide ions of different low coordination, namely $O^{2-}{}_{LC}$ sites.[27]

According to Tench et al.[23] and Zecchina et al.,[24] the absorption of UV light on high-surface-area MgO leads to the formation of surface excitons, whereas the emission of light is associated with the reverse process:

$$h\nu + Mg^{2+}{}_{LC}O^{2-}{}_{LC} \rightleftarrows Mg^{+}{}_{LC}O^{-}{}_{LC}$$

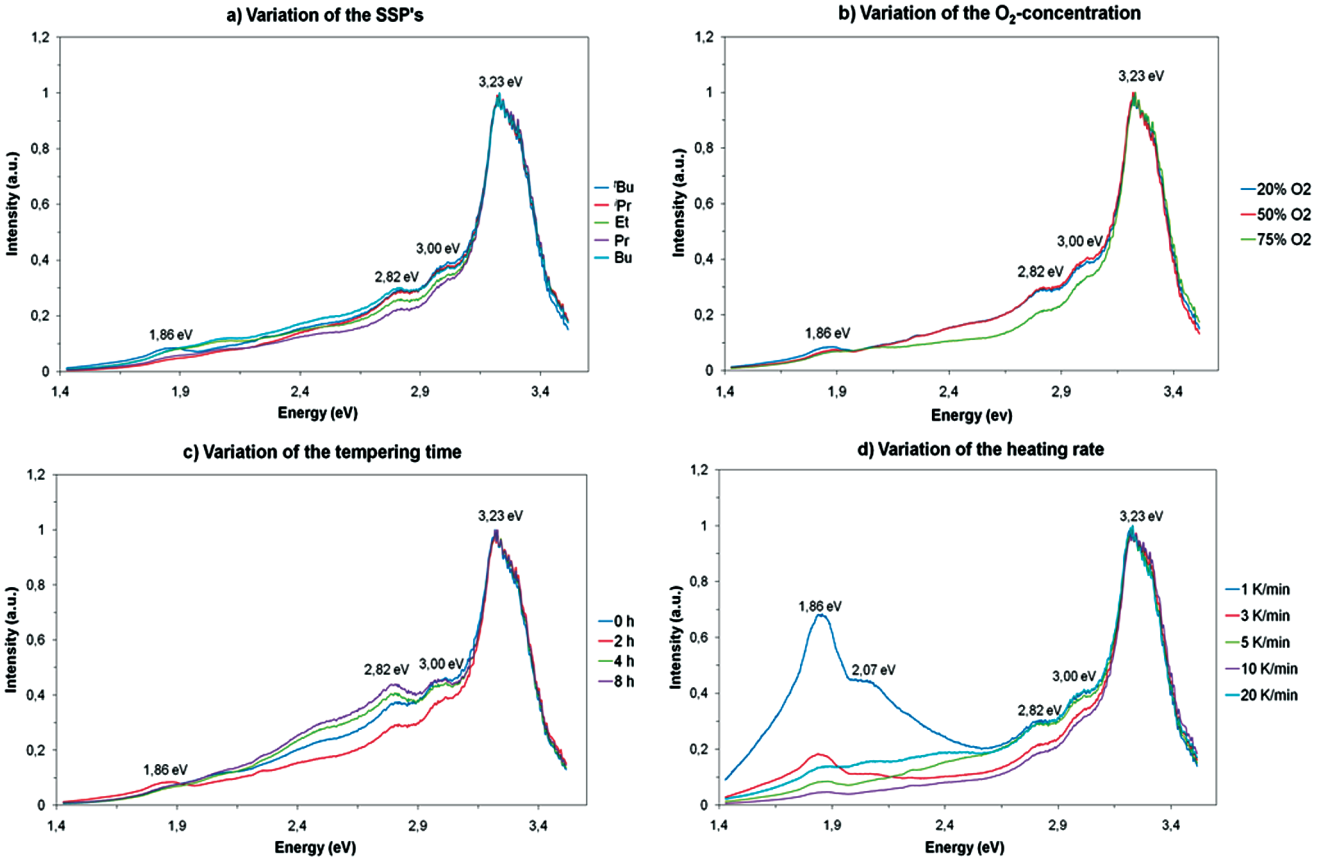

Figure 8. PL spectra of as-prepared MgO nanopowders: (a) from different single-source precursors (SSPs) (**1a**,**b**; **2a**−**c**) (20% O_2; 80% N_2; RT→600 °C (2 h); 5 K/min). MgO derived from **1c** was not measured because of the high carbon impurities; (b) from **1b** under different oxygen concentrations (RT → 600 °C (2 h); 5 K/min); (c) from **1b** applying different calcination times (20% O_2; 80% N_2; RT → 600 °C; 5 K/min) and (d) from **1b** under different heating rates (20% O_2; 80% N_2; RT → 600 °C (2 h)).

The lower the coordination of the surface O^{2-} ions, the lower the Madelung constant and band gap and thus the energy of the luminescence band.[23] The PL spectra of the prepared MgO samples are displayed in Figure 8.

As shown in Figure 8, the MgO samples have been excited with UV light (λ_{max} = 325 nm; 3.8 eV) which resulted in a broad luminescence band at 384 nm (3.2 eV) along with two smaller shoulders at 413 (3.0 eV) and 440 nm (2.8 eV).

Interestingly, a higher oxygen concentration during the thermolysis process (75% O_2, 25% N_2) leads to a significant decrease in the PL signals at 413 and 440 nm, whereas prolonged calcination times result in an increase of the shoulder signals. Moreover, the intensity is slightly influenced by applying different SSPs. The as-prepared MgO from SSPs with relatively bulky alkoxy groups (**1a**, **1b**, and **2c**) show almost similar intensities for their observed PL bands. In contrast, MgO prepared from SSPs with smaller alkoxides (**2a** and **2b**) exhibits less intensive bands at 413 and 440 nm. The MgO samples prepared from **1b** also show a very weak red luminescence at 666 nm (1.86 eV). This band is drastically increased by decomposition of **1b** at relatively low heating rates (1 K/min and 3 K/min, respectively). Under these conditions, an additional broad shoulder appears at 600 nm (2.1 eV).

Because of the lack of theoretical and experimental data in the literature with regard to luminescence of MgO, it is difficult to assign these bands to a certain type of surface defects. In the case of red luminescence, Remón et al. described an emission band centered at 695 nm (1.8 eV) by exciting deformed MgO single particles with 340 nm light.[28] This emission is close to the signal at 666 nm (1.9 eV); however, the same authors suggested that this band may indicate "new defects".

The comparison of the crystal sizes and specific surface areas of the samples prepared with different heating rates reveals that higher heating rates afford larger particles with smaller surface areas. MgO particles that exhibit the largest emission band at 666 nm (1.86 eV) were obtained at the lowest investigated heating rate (1 K/min) and consist of small particles (10.23 nm) with the largest BET surface area (108.2 m^2/g). IR investigations (see the Supporting Information SI-9) show clearly that the surface hydroxide groups and carbonate concentrations can be diminished by decreasing the heating rate, which suggests that surface hydroxide groups and carbon impurities are unlikely as source for the red emission. However, at this stage, we are unable to assign PL signals of the MgO samples to the nature of surface defects. In other words, additional theoretical studies and further spectroscopic measurements are needed for an unambiguous assignment of PL bands and oxide surface defects of the samples. Respective investigations are in progress.

Experimental Section

General Remarks. All reactions were performed under anaerobic conditions using Standard Schlenk techniques. Solvents and alcohols were refluxed over an appropriate drying agent, distilled, degassed, and N_2-saturated prior to use. All other chemicals were used as received commercially from Merck, Alfa Aesar or Acros Organics without further purification. Me_2Mg was prepared as described in literature.[29] The NMR spectra (TMS standard) were recorded on Bruker ARX 200 (1H, 200 MHz; ^{13}C, 50 MHz) and ARX 400 (^1H, 400 MHz; ^{13}C, 100.64 MHz;) spectrometers at ambient temperature.; Elemental analyses were performed on a Perkin-Elmer Series II CHNS/O Analyzer 2400; because of the enormous air-sensitivity of **1a**−**c** and **2a**−**c**, no correct elemental analyses could be measured for **1a**,**c** and **2c**.

Preparation of $[MeMgO^iPr]_4$ (1a). 7.76 g (129 mmol) of ^{i}PrOH were slowly added to a suspension of 7.02 g of (129 mmol) of Me_2Mg in 200 mL of toluene at −78 °C. After 2 h fo stirring, the reaction mixture was allowed to warm to room temperature and then boiled for 48 h. Subsequently, the suspension was filtrated and all volatiles were removed in vacuo. Recrystallization of the residue from hexane at −20 °C affords **1a** as colorless crystals. Yield: 5.30 g (13.5 mmol; 42%). M.p.: 300 °C (decomposition). ^1H NMR (C_6D_6): δ = 3.78 (sept, J = 6.2 Hz, 1H, CH(C$\underline{H}_3$)$_2$); 1.17 (d, J = 6.2 Hz, 6H, CH(C$\underline{H}_3$)$_2$); −0.84 ppm (s, 3H, −C$\underline{H}_3$). ^{13}C {^1H}-NMR (C_6D_6): δ = 66.2 (C$\underline{H}$(CH$_3$)$_2$); 27.0 (CH(C$\underline{H}_3$)$_2$); −15.4 ppm (CH$_3$). $C_{16}H_{40}Mg_4O_4$ (393.71) calcd: C, 48.81; H, 10.24. Found: C, 47.62; H, 9.55.

Preparation of $[MeMgO^tBu]_4$ (1b). In analogy to the synthesis of **1a**, a solution of 10.24 g (188.3 mmol) of Me_2Mg in 250 mL of Et_2O was slowly treated with 13.69 g (188.3 mmol) to give **1b** as white solid. Yield: 20.65 g (45.91 mmol; 98%). M.p.: 308 °C (decomposition). ^1H NMR (C_6D_6): δ = δ = 1.35 (s, 9H, C(CH$_3$)$_3$); −0.73 ppm (s, 3H, CH$_3$). $^{13}C\{^1H\}$-NMR (C_6D_6): δ = 72.6 (C(CH$_3$)$_3$); 32.4 (C(C$\underline{H}_3$)$_3$); −11.4 ppm (CH$_3$). $C_{20}H_{48}Mg_4O_4$ (449.81) calcd: C, 53.40; H, 10.76. Found: C, 52.64; H, 10.35.

Preparation of $[MeMgO^{Cy}Hex]_4$ (1c). In analogy to the synthesis of **1a**, 7.38 g (73.6 mmol) ^{Cy}HexOH were slowly added to a suspension of 4.00 g (73.6 mmol) of Me_2Mg in 250 mL of toluene at −78 °C. Analogous workup and recrystallization from hot toluene affords **1c** as colorless needles. Yield: 5.93 g (10.7 mmol; 58%). M.p.: 290 °C (decomposition). ^1H NMR (C_6D_6): δ = 3.65; 2.30; 1.52; 1.34; 0.99 (m, 11H, ^{Cy}Hex); −0.70 ppm (s, 3H, CH$_3$).^{13}C {^1H} NMR (C_6D_6): δ = 72.9; 38.8; 25.2 (^{Cy}Hex); −14.5 ppm (CH$_3$). $C_{28}H_{56}Mg_4O_4$ (553.96) calcd: C, 60.71; H, 10.19. Found: C, 58.92; H, 9.56.

Preparation of $Me_6Mg_7(OEt)_8$ (2a). In analogy to the synthesis of **1a**, 4.19 g (90.9 mmol) of EtOH was slowly added to a suspension of 4.94 g (90.9 mmol) of Me_2Mg in 250 mL of toluene at −78 °C. Analogous workup and recrystallization from toluene at −78 °C affords **2a** as colorless crystals. Yield: 6.24 g (10.1 mmol; 78%). M.p.: 241 °C. ^1H NMR (C_6D_6): δ = 3.72 (q, J = 7.0 Hz, 12H, -C$\underline{H}_2$CH$_3$); 3.63 (q, J = 7.0 Hz, 4H, -C$\underline{H}_2$CH$_3$); 1,21 (t, J = 7.0 Hz, 18H, CH$_2$C$\underline{H}_3$); 1.13 (t, J = 7.0 Hz, 6H, CH$_2$C$\underline{H}_3$); −0.96 ppm (s, 18H, C$\underline{H}_3$). $^{13}C\{^1H\}$ NMR (C_6D_6): δ = 59.1; 58.7 (C$\underline{H}_2$CH$_3$); 20.8; 20.6 (CH$_2$C$\underline{H}_3$); −17.6 ppm (C$\underline{H}_3$). $C_{22}H_{58}Mg_7O_8$ (620.83) calcd: C, 42.56; H, 9.42. Found: C, 42.02; H, 8.92.

Preparation of $Me_6Mg_7(OPr)_8$ (2b). In analogy to the synthesis of **2a**, the reaction of 6.47 g (108 mmol) ^{n}PrOH with 5.85 g (108 mmol) Me_2Mg in toluene, analogous workup and recrystallization from hexane at −20 °C affords **2b** as colorless crystals. Yield: 9.54 g (13.0 mmol; 96%). M.p.: 246 °C. ^1H NMR (C_6D_6): δ = 3.82 (t, J = 7.6 Hz, 12H, -C$\underline{H}_2$CH$_2$CH$_3$); 3.63 (t, J = 7.6 Hz, 4H, C$\underline{H}_2$CH$_2$CH$_3$); 1.76 (m, 12H, CH$_2$C$\underline{H}_2$-CH$_3$); 1.67 (m, 4H, CH$_2$C$\underline{H}_2$CH$_3$); 0. of 84 (t, J = 7.4 Hz, 18H, −CH$_2$CH$_2$C$\underline{H}_3$); 0.70 (t, J = 7.4 Hz, 6H, CH$_2$CH$_2$C$\underline{H}_3$); −0.87 ppm (s, 18H, C$\underline{H}_3$). $^{13}C\{^1H\}$ NMR (C_6D_6): δ = 66.0; 65.7 (C$\underline{H}_2$CH$_2$CH$_3$); 28.4; 28.2 (CH$_2$C$\underline{H}_2$CH$_3$); 10.3; 10.1 (CH$_2$CH$_2$ C$\underline{H}_3$); −16.8 ppm (C$\underline{H}_3$). $C_{30}H_{74}Mg_7O_8$ (733.04) calcd: C, 49.15; H, 10.18. Found: C, 48.70; H, 9.66.

Preparation of $Me_6Mg_7(OBu)_8$ (2c). In analogy to the synthesis of **1a**, 6.47 g (108 mmol) BuOH were slowly added to a suspension of 5.85 g (108 mmol) of Me_2Mg in 250 mL toluene at −78 °C. Analogous workup and recrystallization from hexane at −20 °C affords **2c** as colorless crystals. Yield: 7.42 g (8.78 mmol; 74%). M. p.: 248 °C. ^1H NMR (C_6D_6): δ = 4.00 (t, J = 7.5 Hz, 12H, C$\underline{H}_2$CH$_2$CH$_2$CH$_3$); 3.96 (t, J = 7.5 Hz, 4H, C$\underline{H}_2$CH$_2$CH$_2$CH$_3$); 1.86 (m, 12H, CH$_2$C$\underline{H}_2$CH$_2$CH$_3$); 1.71 (m, 4H, CH$_2$C$\underline{H}_2$CH$_2$CH$_3$); 1.38 (m, 12H, CH$_2$CH$_2$C$\underline{H}_2$CH$_3$); 1.17 (m, 4H, CH$_2$CH$_2$C$\underline{H}_2$CH$_3$); 0.91 (t, J = 7.4 Hz, 18H, CH$_2$CH$_2$-CH$_2$C$\underline{H}_3$); 0.82 (t, J = 7.4 Hz, 6H, CH$_2$CH$_2$CH$_2$C$\underline{H}_3$); −0.80 ppm (s, 18H, CH$_3$). $^{13}C\{^1H\}$ NMR (C_6D_6): δ = 64.3; 63.8 (C$\underline{H}_2$-CH$_2$CH$_2$CH$_3$); 37.3; 37.2 (CH$_2$C$\underline{H}_2$CH$_2$CH$_3$); 19.8; 19.4 (C$\underline{H}_2$-CH$_2$C$\underline{H}_2$CH$_3$); 13.9; 13.8 (C$\underline{H}_2$CH$_2$CH$_2$C$\underline{H}_3$); −16.8 ppm (C$\underline{H}_3$). $C_{38}H_{90}Mg_7O_8$ (845.25) calcd: C, 54.00; H, 10.73. Found: C, 52.35; H, 10.16.

Single-Crystal X-ray Structure Determinations. Crystals were each mounted on a glass capillary in perfluorinated oil and measured in a cold steam of N_2. The data for **1a** and **2b** were collected with a Bruker-AXS SMART CCD diffractometer (MoK_α radiation, λ = 0.71707 Å, ω-Scan). The structures were solved by direct methods. Refinement were carried out with the SHELXL-97 package.[33] All thermal displacement parameters were refined anistropically for non-H atoms and isotropically for H atoms. All refinements were made by full matrix least-squares on F^2. CCDC 763822 (1a) − 763823 (2b) contains the supplementary crystalographic data for this paper. These data can be ontained free of charge via www.ccdc.cam.ac.uk/data_request/cif, or by emailing data_requst@ccdc.cam.ac.uk, or by contacting The Cambridge Crystallographic Data Centre, 12, Union Road, Cambridge CB2 1EZ, UK; Fax: +44 1223 336033.

Crystal Data for ***1a***. $C_{16}H_{40}Mg_4O_4$, M = 393.72; monoclinic, space group $P2/n$; a = 9.5351(18) Å, b = 9.4676(16) Å, c = 14.329(4) Å, $\alpha = \gamma = 90°$, β = 107.82(2)°, V = 1231.5(5) Å^3; D_c (Z=2) = 1.062 g cm^{-3}; T = 150 K, 2158 reflections with $I > 2\sigma(I)$, θ_{max} = 24.99°, R_1 = 0.0847 (observed reflections), wR_2 = 0.1337 (all data) (see also the Supporting Information).

Crystal Data for ***2b***. $C_{30}H_{74}Mg_7O_8$, M = 733.06; triclinic, space group $P\bar{1}$; a = 10.2934(6) Å, b = 10.8204(4) Å, c = 11.5065(6) Å, α = 79.617(4)°, β = 68.439(5)°, γ = 74.077(4)°, V = 1141.64(11) Å^3; D_c (Z = 1) = 1.066 g cm^{-3}; T = 150 K, 3998 reflections with $I > 2\sigma(I)$, θ_{max} = 25.00°, R_1 = 0.0539 (observed reflections), wR_2 = 0.1425 (all data) (see also the Supporting Information).

Nanoparticle Preparation. Nanocrystalline MgO was prepared by thermolysis of alkyl-Mg-alkoxides $[MeMgOR]_4$ (R = ^{i}Pr, ^{t}Bu, ^{Cy}Hex) and $Me_6Mg_7OR_8$ (R = Et, Pr, Bu) in a quartz tube reactor. Unless indicated otherwise, the decomposition was carried out in synthetic air (20% O_2, 80% N_2) and the heating rate toward the final temperature (600 °C) was 5K min^{-1} with a subsequent heating time of 2 h at 600 °C. Commercially available MgO (Aldrich, 99.99%, metals basis) was used as a reference material for comparison.

Analytical Methods. FT-IR spectra were recorded from KBr pellets by using a Bruker Vektor 22 spectrometer. X-ray Powder

Diffractograms were performed on a Bruker AXS D8 Advance instrument using $Cu_{K\alpha}$ radiation (λ = 1.5418 Å) and a position-sensitive detector (PSD) in the 2θ range from 25 to 85° with a 0.015° step. Crystallite size and microstrain parameters were determined by performing a full profile Warren-Averbach fit of experimental PXRD patterns with subsequent decomposition of reflection profiles into Gaussian and Lorenzian parts, taking into account instrumental contribution to peak broadening. Photoluminescence spectra (PL) were recorded at room temperature using a fiber-coupled Czerny-Turner spectrograph and an attached UV−vis CCD camera (Andor Technology, SR-303i and DU401-BR, respectively) located at the Helmholtz-Zentrum, Berlin. A simple copper plate, which does not show significant emissions under UV excitation, was used as sample holder for the prepared nanopowders. The diameter of the optical fiber was 600 μm, and a 150 grooves/mm grating was applied. The focused UV light (lambda = 325 nm) of a He−Cd laser (Kimmon Koha Co., IK 5651R-G) served as the excitation illumination. In order not to destroy the detector, an appropriate edge filter was used to block the excitation light. The spectral response of the detection system was then accurately calibrated with a tungsten-wire calibration source. Elemental analysis was performed on a Perkin-Elmer 2400 CHN-S/O elemental analyzer. Thermogravimetric analysis (TGA) of the precursor was carried out with a thermogravimetric setup from Rubotherm under synthetic air ($20\%O_2$-$80\%N_2$) and with a heating rate of 5 K/min. The specific BET surface areas were measured using nitrogen adsorption at 77 K with a micromeritics Gemini III 2375 Surface Area Analyzer.

Scanning electron microscopy (SEM) images were acquired using a Hitachi S-4000 microscope equipped with an SAMX EDX detector. The SEM samples were prepared by shortly dipping a carbon carrier in the solution, where MgO particles were dispersed in acetone. The EDX samples were measured on carbon coated Cu-TEM grids. Transmission Electron Microscopy (TEM) images were recorded on a tecnai G^2 20 S-TWIN (operating at 10 keV) with an energy dispersive X-ray spectrometer (EDAX, r-TEM SUTW) located at the ZELMI, TU Berlin.

Acknowledgment. We thank the Cluster of Excellence "Unifying Concepts in Catalysis" (sponsored by the Deutsche Forschungsgemeinschaft and admistered by the Technische Universität Berlin) for financial support. We thank also Prof. M. Lehmann and ZELMI (Zentrales Laboratorium für Elektronenmikroskopie, TU Berlin) for TEM analyses and Dr. T. Schedel-Niedrig from Helmholtz Zentrum Berlin for performing the PL spectra and helpful discussions.

Supporting Information Available: Further details on the single-crystal XRD characterization of the precursors **1a** and **2b**, TGA-DTG (of **1a**, **1c**, **2a**−**c**), and TGA-MS (of **1a**−**b**, **2b**) as well as information concerning the characterization of the prepared MgO samples such as PXRD (for **1c**, **2a**−**c**, and the degradation of **1b** under different conditions), TEM (for **1a**−**c**, **1b** decomposed with different heating rates, **2a**, and **2c**), EDX (for **1b** and **2b**), and IR (for **1b** decomposed with different heating rates) measurements (PDF). This material is available free of charge via the Internet at http://pubs.acs.org/.